IEEE Access
Multidisciplinary | Rapid Review | Open Access Journal

Received July 31, 2020, accepted August 15, 2020, date of publication August 18, 2020, date of current version August 28, 2020.

Digital Object Identifier 10.1109/ACCESS.2020.3017621

Multibeam Single-Sideband Time-Modulated Arrays

ROBERTO MANEIRO-CATOIRA, (Member, IEEE), JOSÉ A. GARCÍA-NAYA, (Senior Member, IEEE), JULIO C. BRÉGAINS, (Senior Member, IEEE), AND LUIS CASTEDO, (Senior Member, IEEE)

CITIC Research Center, Department of Computer Engineering, University of A Coruña, 15071 A Coruña, Spain

Corresponding author: José A. García-Naya (jagarcia@udc.es)

This work was supported in part by the Xunta de Galicia under Grant ED431G2019/01; in part by the Agencia Estatal de Investigación of Spain under Grant TEC2016-75067-C4-1-R, Grant RED2018-102668-T, and Grant PID2019-104958RB-C42; and in part by European Regional Development Fund (ERDF) Funds of the European Union (EU) (FEDER Galicia and Agencia Estatal de Investigación (AEI)/FEDER, EU).

ABSTRACT The design of efficient time-modulated arrays (TMAs) for multi-beam steering purposes must be based on both a type of periodical sequences that guarantees an adequate windowing of exploited harmonics, and a feeding network capable of providing low hardware insertion losses. Compliance with these two requirements is not simple and is aggravated by the fact that, as the number of exploited harmonic beams increases, not only drastically decreases the antenna efficiency, but also the beam steering flexibility. In this work, we propose three different single sideband (SSB) feeding networks for multibeam TMAs constructed considering different combinations of single-pole multiple-throw (SPMT) basic modules. The proposed feeding networks simultaneously accomplish excellent levels of modulation efficiency, reasonable hardware insertion losses, and beam scanning flexibility. In addition, a comparison with standard phased arrays in terms of performance, phase sensitivity, complexity, and cost-effectiveness is carried out.

INDEX TERMS Time-modulated arrays, beam steering, multibeam.

I. INTRODUCTION

A time-modulated array (TMA) is an adaptive antenna array whose radiation pattern is controlled by suitably varying in time the excitations of its individual array elements [1]. Time-modulation is typically implemented with radio frequency (RF) switches which apply periodical pulses (with fundamental period T_0) to the individual array excitations. As a result, TMAs generate radiation patterns at the harmonic frequencies $\omega_c \pm q\omega_0$, with $q \in \{1, 2, 3, \ldots\}$, ω_c being the carrier frequency, and $\omega_0 = 2\pi/T_0$ [2]. TMAs have significant differentiating features when compared to standard phased arrays, namely:

- A lower cost of the array feeding network due to the utilization of RF switches instead of more expensive variable phase shifters (VPSs) [3]–[5], with the cost gap increasing with the carrier frequency. In this sense, the performance of the TMA switches is conditioned by the signal bandwidth [6], whereas that of the VPSs is dominated by the carrier frequency.
- An accurate and simple way to electronically steer the antenna beampattern by modifying the on-off switching instants [7], [8].
- The ability to transform spatial diversity into frequency diversity, which opens the possibility to implement smart antenna extra functionalities such as angle diversity reception in multipath wireless channels [9], multiuser communications [10], [11] (both with the benefit of employing a single RF front-end), direction finding [12], [13], or secure signal transmissions [14], [15].

However, in spite of their clear advantages, further efforts are still necessary to improve the efficiency and flexibility of switched TMAs for simultaneously handling multiple beampatterns. As a matter of fact, the early attempts to design multibeam TMAs were based on the application of one single-pole single-throw (SPST) switch per antenna element, which showed the following drawbacks: 1) the lack of efficiency of rectangular pulses when distributing the spectral energy among the working and undesired harmonics [16]; 2) the wasting of certain amount of energy of transmitted/received signals during the zero-state of the switches [17]; 3) the presence of frequency-mirrored radiation patterns at the negative-frequency harmonics [18]; and 4) the

The associate editor coordinating the review of this manuscript and approving it for publication was Muhammad Zubair.

proportionality between the harmonic phases, which limits their multiple beam steering capability [15].

Alternative TMA approaches with single-pole multiple-throw (SPMT) switches have been subsequently considered [7], [9], [19]. However, these approaches provide a low-loss feeding network at the expense of a modest harmonic windowing [7], [19] or, conversely, they exhibit a suitable harmonic windowing at the cost of high-loss feeding networks [9].

The main contribution of this paper is the consideration of RF SPMT switches for the construction of TMA feeding networks capable of efficiently steering multiple beam patterns simultaneously. Three different TMA feeding networks with distinct steering capabilities will be considered and constructed from different combinations of two types of basic feeding network modules: one implemented with single-pole double-throw (SPDT) switches, and the other one implemented with single-pole triple-throw (SP3T) switches. All feeding networks are of the single sideband (SSB) type in the sense that they are able to remove the harmful frequency-mirrored beam patterns produced by conventional TMAs.

Up to the authors' knowledge, no previous study has addressed the design of SSB multibeam switched TMAs, being the state of the art focused on the design of single-beam SSB TMA feeding networks [8], [20], [21] or simply replicating the hardware of a such single-beam feeding networks to simultaneously handle multiple beams [11]. The beam steering features of the three proposed multibeam SSB TMA approaches are evaluated in terms of time-modulation radiation efficiency (closed-form expressions are determined) and hardware efficiency estimates. Finally, we present a comparative analysis with standard multibeam phased arrays in terms of performance, complexity, phase sensitivity, and cost-effectiveness.

II. TWO INDEPENDENTLY-STEERABLE BEAMS

The first SSB TMA feeding network considered allows for independently steering two harmonic beam patterns. The approach is constructed with three SPDT modules as explained in the ensuing subsections.

A. SPDT MODULE

Let us start considering a receive linear TMA with N isotropic[1] elements and unitary static excitations, i.e., $I_n = 1$, $n \in \{0, 1, \ldots, N-1\}$. Let us next consider that these array excitations are time-modulated with the periodical (T_0) extension of the pulsed waveform $p(t)$ plotted in Fig. 1. Such a periodical extension admits the exponential Fourier series representation $\sum_{q=-\infty}^{\infty} P_q e^{jq\omega_0 t}$, where $\omega_0 = 2\pi/T_0$

[1]When novel TMA approaches are analyzed, as a general rule, isotropic elements are assumed (e.g., [15], [18], [22]–[25]) in order to both reduce the complexity of the analysis and to focus on the effects of the applied time modulation technique.

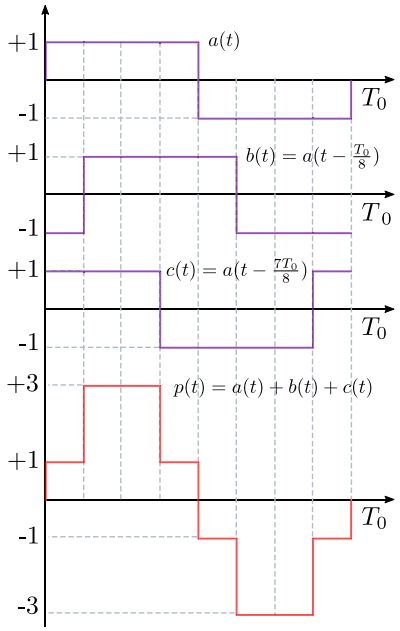

FIGURE 1. Single period (T_0) time-modulating pulsed waveforms $a(t)$, $b(t) = a(t - T_0/8)$, $c(t) = a(t - 7T_0/8)$, and $p(t) = a(t) + b(t) + c(t)$.

and P_q, $q \in \mathbb{Z}$, are the Fourier coefficients

$$P_q = \frac{1}{T_0}\int_0^{T_0} p(t)e^{-jq\omega_0 t} = \begin{cases} \dfrac{2 - 2\sqrt{2}\cdot(-1)^{\frac{(q+3)(q+5)}{8}}}{j\pi q} & \text{for } q \text{ odd} \\ 0 & \text{for } q \text{ even} \end{cases} \quad (1)$$

The mean square value of $p(t)$ is

$$\mathcal{P}_p = \frac{1}{T_0}\int_0^{T_0} p^2(t)dt = \sum_{q=-\infty}^{\infty} |P_q|^2 = 5 \quad (2)$$

Fig. 1 also shows how $p(t)$ may be synthesized as the sum of the three bipolar square pulses $a(t)$, $b(t) = a(t - T_0/8)$, and $c(t) = a(t - 7T_0/8)$. Note that time modulation with a bipolar square pulse is readily implementable with an SPDT switch and a fixed π delay line, reversing the signal sign of one of the dual throws. Fig. 2 shows the feeding network that modulates $p(t)$ in time, with the RF input signal $s(t)$ received at an antenna element. The 3-way power splitter divides $s(t)$ into three equal-powered replicas and each one is time-modulated with $a(t)$, $b(t)$, and $c(t)$, respectively. Note that the three SPDT switches in Fig. 2 are controlled with time-shifted versions of the same unipolar signal $g(t)$ defined as

$$g(t) = \begin{cases} 1 & a(t) \geq 0 \\ 0 & a(t) < 0 \end{cases} \quad (3)$$

The individual time-modulated signals are subsequently combined (with a 3-way power combiner) to produce the output

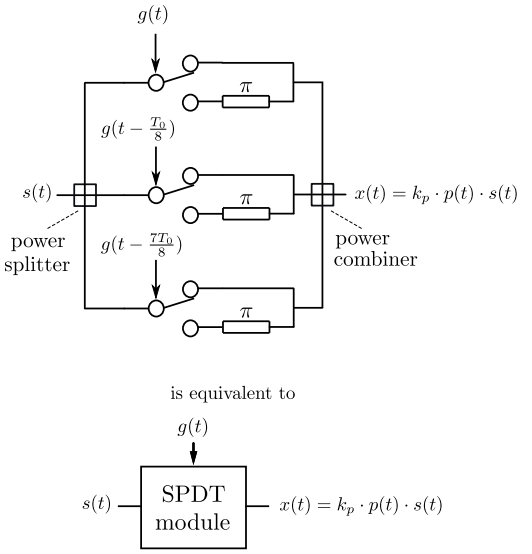

FIGURE 2. SPDT feeding network that time modulates the input signal $s(t)$ with the pulsed waveform $p(t)$ (top) and its equivalent block diagram (bottom).

signal $x(t) = k_p p(t)s(t)$, where k_p is a proportionality constant accounting for the possible attenuation introduced by the feeding network.

Let $s(t)$ be a band-limited input signal with passband bandwidth B_s Hz, power spectral density (psd) $\Phi_{ss}(f)$ [W/Hz], and total time-averaged power $\mathcal{P}_s = \int_{-\infty}^{\infty} \Phi_{ss}(f)df$. The psd of $x(t) = k_p p(t)s(t)$ is

$$\Phi_{xx}(f) = k_p^2 \sum_{q=-\infty}^{\infty} |P_q|^2 \Phi_{ss}(f - qf_0),\ f_0 = 1/T_0 \qquad (4)$$

Assuming $f_0 > 2\,B_s$, the shifted replicas of $\Phi_{ss}(f)$ in $\Phi_{xx}(f)$ do not overlap and the total time-averaged power of $x(t)$ is

$$\mathcal{P}_x = \int_{-\infty}^{\infty} \Phi_{xx}(f)df = k_p^2 \sum_{q=-\infty}^{\infty} |P_q|^2 \mathcal{P}_s = k_p^2 \mathcal{P}_p \mathcal{P}_s \qquad (5)$$

being $\mathcal{P}_p$ the parameter obtained in (2). Contrarily to conventional TMAs implemented with SPST on-off switches, the SPDT module in Fig. 2 is able to theoretically deliver all the input power to the output since there is no off-state in the switches that waste power. Assuming that all the hardware elements in the feeding network are ideal and have no insertion losses, then $\mathcal{P}_x = \mathcal{P}_s$, and $k_p^2 = 1/\mathcal{P}_p = 1/5$.

The SPDT feeding network is abstracted in the block diagram named "SPDT module" (shown at the bottom in Fig. 2) to be employed as the building block of the more sophisticated SSB TMA approach considered in the ensuing subsection.

The pulsed waveform $p(t)$ has been selected because of its particular spectral characteristics. Fig. 3 plots $20\log|\frac{P_q}{P_1}|$, i.e., the Fourier series mean square spectrum of $p(t)$ normalized with respect to P_1. In view of Fig. 3, the harmonics with $|q| = 1$ are the most relevant and will be selected to handle the useful signal. The remaining harmonics ($|q| \neq 1$)

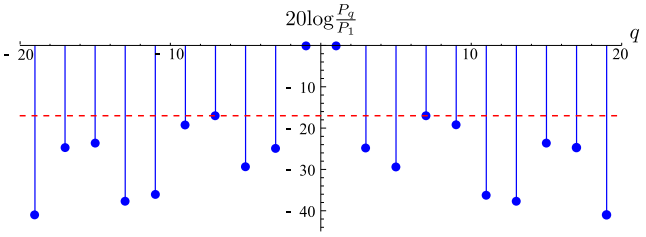

FIGURE 3. Normalized Fourier series mean square spectrum in dB, $10\log_{10}\left|\frac{P_q}{P_1}\right|^2$, of the periodical extension of the stair-step pulse $p(t)$ in Fig. 1. The relative level of the harmonics with $|q = 7|$ is -16.9 dB and is emphasized with the dashed red line.

will be considered unwanted. According to Fig. 3, the most meaningful undesirable harmonics are those with order $|q| = 7$, which have a relative level of -16.9 dB (correspondingly indicated with a dashed red line).

B. SSB TMA FEEDING NETWORK

The SPDT module described in the previous subsection will be used to construct the SSB TMA feeding network plotted in Fig. 4 for a single antenna element. In what follows, we will explain how this feeding network is able to independently steer two antenna array beams by properly selecting the time-delay parameters D_{1n} and D_{2n} shown in Fig. 4.

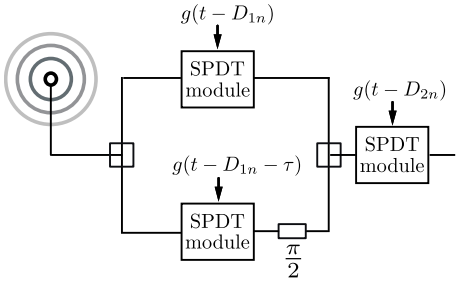

FIGURE 4. Block diagram of the n^{th} element feeding network of the SSB TMA approach that allows for steering independently two harmonic beam patterns.

According to Fig. 4, the signal collected by the n-th antenna element is split into two branches by means of a 2-way splitter. The upper branch has an SPDT module whose control signal is $g(t - D_{1n})$, being D_{1n} a time delay. The lower branch consists of an SPDT module –having a control signal $g(t - D_{1n} - \tau)$, with τ being a fixed time delay such that $\omega_0\tau = \pi/2$ [9]– followed by a $\pi/2$ phase shifter. The signals from the two branches are combined with a 2-way combiner whose output goes through a third SPDT module with control signal $g(t - D_{2n})$, being D_{2n} an additional time delay. Observe how the block diagram in Fig. 4 resembles that of an SSB modulation, and hence the term SSB denotes a TMA whose signals are time modulated with the feeding network in Fig. 4.

The radiation directional characteristics of an antenna array are determined by its array factor. A distinctive feature of a TMA is that its array factor is time-variant. Indeed, the time-variant array factor of a linear TMA with time modulated excitations $h_n(t)$, $n \in \{0, \ldots N-1\}$, and the

term $e^{j\omega_c t}$ explicitly included, is

$$F(\theta, t) = e^{j\omega_c t} \sum_{n=0}^{N-1} h_n(t) e^{j\beta_c z_n \cos\theta} \tag{6}$$

where z_n represents the position of the n-th array ideal (i.e., perfectly conductive) isotropic element on the z axis, θ is the angle with respect to such a main axis, and $\beta_c = 2\pi/\lambda_c$ is the wavenumber for a carrier wavelength $\lambda_c = 2\pi c/\omega_c$, being ω_c the carrier frequency.

According to Fig. 2 and 4, the time modulated excitations are

$$h_n(t) = \left[\frac{k_p p(t - D_{1n})}{\sqrt{2}} + j\frac{k_p p(t - D_{1n} - \tau)}{\sqrt{2}}\right] \cdot k_p p(t - D_{2n}) \tag{7}$$

As explained below, the time delays D_{1n} and D_{2n} are instrumental to determine the steering directions of the two-beams in the considered SSB TMA.

From the Fourier series expansion of the time-shifted versions of $p(t)$, $h_n(t)$ in (7) can be rewritten as

$$h_n(t) = \frac{k_p^2}{\sqrt{2}} \left[\sum_{q \text{ odd}} \left(1 - (-j)^{q+1}\right) P_q e^{-jq\omega_0 D_{1n}} e^{jq\omega_0 t}\right] \cdot \left[\sum_{i \text{ odd}} P_i e^{-ji\omega_0 D_{2n}} e^{ji\omega_0 t}\right] \tag{8}$$

where i belongs to the set of odd integers, and we have taken into account that $e^{-jq\omega_0\tau} = (-j)^q$ as a consequence of $\omega_0\tau = \pi/2$. We now define the set $\Psi = \{4\Gamma - 3\}$ with $\Gamma \in \mathbb{Z}$, and see that

$$1 - (-j)^{q+1} = \begin{cases} 2 & q \in \Psi \\ 0 & \text{otherwise} \end{cases} \tag{9}$$

which allows us to rewrite $h_n(t)$ in (8) as

$$h_n(t) = \sqrt{2}k_p^2 \left[\sum_{q \in \Psi} P_q e^{-jq\omega_0 D_{1n}} e^{jq\omega_0 t}\right] \cdot \left[\sum_{i \text{ odd}} P_i e^{-ji\omega_0 D_{2n}} e^{ji\omega_0 t}\right] \tag{10}$$

To simplify the notation, we now define the dynamic excitations as

$${}_i^q I_n = \sqrt{2}k_p^2 P_q P_i e^{-j\omega_0(qD_{1n} + iD_{2n})} \tag{11}$$

simplifying equation (10) to

$$h_n(t) = \sum_{q \in \Psi} \sum_{i \text{ odd}} {}_i^q I_n e^{j(q+i)\omega_0 t}. \tag{12}$$

Finally, substituting (12) into (6) we arrive at the time-variant array factor

$$\begin{aligned} F(\theta, t) &= \sum_{q \in \Psi} \sum_{i \text{ odd}} \sum_{n=0}^{N-1} {}_i^q I_n e^{j\beta_c z_n \cos\theta} e^{j(\omega_c + (q+i)\omega_0)t} \\ &= \sum_{q \in \Psi} \sum_{i \text{ odd}} F_i^q(\theta) e^{j(\omega_c + (q+i)\omega_0)t} \end{aligned} \tag{13}$$

where

$$F_i^q(\theta) = \sum_{n=0}^{N-1} {}_i^q I_n e^{j\beta_c z_n \cos\theta} \tag{14}$$

is the spatial array factor at the frequency $\omega_c + (q + i)\omega_0$. (13) indicates that the proposed TMA radiates replicas of $s(t)$ around the frequencies $\omega_c + (q+i)\omega_0$, which are $(q+i)$ integer multiples of the TMA fundamental frequency ω_0 centered around the carrier frequency ω_c.

Notice that the moduli of the dynamic excitations $|{}_i^q I_n|$ are constant for all n (see (11) and (1)), whereas their phases $\sphericalangle {}_i^q I_n$ depend on $qD_{1n} + iD_{2n}$. Therefore, the radiated power pattern of any harmonic –obtained through $10\log|F_i^q(\theta)|^2$– corresponds to that of a uniform linear array and such patterns can be steered by adapting the phase terms $qD_{1n} + iD_{2n}$.

In view of (11) and the harmonics profile in Fig. 3, we observe that the most meaningful harmonic patterns in (13), in decreasing order of significance, are the ones shown in Table 1. We define ${}_i^q\Delta_{\text{peak}}$ as the relative level of the maximum of a given harmonic pattern $|F_i^q(\theta_{\max})|$ with respect to the maximum of $|F_1^1(\theta_{\max})|$, which we take as a reference pattern, i.e., ${}_i^q\Delta_{\text{peak}} = 20\log|F_i^q(\theta_{\max})/F_1^1(\theta_{\max})|$. $\theta_{\max}$ represents the direction in which an array factor amplitude is a maximum. According to Table 1, the useful harmonics are $\omega_c + 2\omega_0$ (i.e., $q = i = 1$) and ω_0 (i.e., $q = 1$ and $i = -1$) because their beam patterns, $F_{-1}^1(\theta)$ and $F_1^1(\theta)$, have a peak level which is 16.9 dB above the remaining ones, i.e., the two beam patterns $F_{-1}^1(\theta)$ and $F_1^1(\theta)$ are the ones that will be used to receive the desired signal, whereas the remaining ones are not worth taking advantage of due to their corresponding low ${}_i^q\Delta_{\text{peak}}$.

TABLE 1. Most meaningful terms in (13) and characteristics of the corresponding harmonic patterns. The useful harmonics are shaded in gray.

q	i	frequency	dynamic excitations (${}_i^q I_n$)	${}_i^q\Delta_{\text{Peak}}$ (dB)
1	1	$\omega_c + 2\omega_0$	$\sqrt{2}k_p^2 P_1^2 \cdot e^{-j\omega_0(D_{1n}+D_{2n})}$	0
1	−1	ω_c	$\sqrt{2}k_p^2 P_1 P_{-1} \cdot e^{-j\omega_0(D_{1n}-D_{2n})}$	0
1	7	$\omega_c + 8\omega_0$	$\sqrt{2}k_p^2 P_1 P_7 \cdot e^{-j\omega_0(D_{1n}+7D_{2n})}$	−16.9
1	−7	$\omega_c - 6\omega_0$	$\sqrt{2}k_p^2 P_1 P_{-7} \cdot e^{-j\omega_0(D_{1n}-7D_{2n})}$	−16.9
−7	1	$\omega_c - 6\omega_0$	$\sqrt{2}k_p^2 P_{-7} P_1 \cdot e^{-j\omega_0(-7D_{1n}+D_{2n})}$	−16.9
−7	−1	$\omega_c - 8\omega_0$	$\sqrt{2}k_p^2 P_{-7} P_{-1} \cdot e^{-j\omega_0(-7D_{1n}-D_{2n})}$	−16.9

C. SSB TMA BEAM STEERING

Let us assume the N antennas of the considered linear SSB TMA to be uniformly spaced $\lambda_c/2$ apart. Hence, $\beta_c z_n = \pi n$ and, according to (14) and (11), the spatial array factors of the useful harmonics simplify to

$$\begin{aligned} F_1^1(\theta) &= \sum_{n=0}^{N-1} \sqrt{2}k_p^2 P_1^2 \cdot e^{j(n\pi\cos\theta - \omega_0(D_{1n}+D_{2n}))}, \\ F_{-1}^1(\theta) &= \sum_{n=0}^{N-1} \sqrt{2}k_p^2 P_1 P_{-1} \cdot e^{j(n\pi\cos\theta - \omega_0(D_{1n}-D_{2n}))} \end{aligned} \tag{15}$$

Hence, if we are willing to steer these beampatterns towards the directions θ_a and θ_b, respectively, the following two conditions must hold

$$\begin{aligned} n\pi\cos\theta_a &= \omega_0(D_{1n}+D_{2n}) \\ n\pi\cos\theta_b &= \omega_0(D_{1n}-D_{2n}), \end{aligned} \tag{16}$$

which lead to the following normalized time delays

$$\begin{aligned} d_{1n} &= \frac{D_{1n}}{T_0} = \frac{n(\cos\theta_a+\cos\theta_b)}{4} \\ d_{2n} &= \frac{D_{2n}}{T_0} = \frac{n(\cos\theta_a-\cos\theta_b)}{4}. \end{aligned} \tag{17}$$

These are the delays for $F_1^1(\theta)$ and $F_{-1}^1(\theta)$ to point towards θ_a and θ_b, respectively. Note how the steering of $F_1^1(\theta)$ and $F_{-1}^1(\theta)$ can be performed independently.

D. RADIATION AND HARDWARE EFFICIENCIES

When handling TMAs, at least two types of power efficiencies should be considered [9], [26]. The first one is the so-called time-modulation radiation efficiency defined as $\eta_{\rm TM} = \mathcal{P}_U^{\rm TM}/\mathcal{P}_R^{\rm TM}$, where $\mathcal{P}_U^{\rm TM}$ is the useful average power radiated over the harmonics exploited by the TMA and $\mathcal{P}_R^{\rm TM}$ is the total average power radiated over all existing harmonics. Recall that TMAs waste the power difference $\mathcal{P}_R^{\rm TM}-\mathcal{P}_U^{\rm TM}$ radiated over the unexploited harmonics.[2] Hence, $\eta_{\rm TM}$ is an efficiency intrinsically linked to the time-modulation operation and its value depends on the specific TMA technique under consideration.

According to [9], the total power radiated by a SSB TMA is

$$\mathcal{P}_R^{\rm TM} = 4\pi\mathcal{P}_s\sum_{n=0}^{N-1}\sum_{q\in\Psi}\sum_{i\ \text{odd}}|{}_i^qI_n|^2, \tag{18}$$

where $\mathcal{P}_s$ is the input power per antenna. Under the assumptions of unitary static excitations and ideal hardware elements with no insertion losses (see Section II.A), the total power radiated simplifies to $\mathcal{P}_R^{\rm TM} = 4\pi N\mathcal{P}_s$.

In this case, the useful power is the one radiated over the two harmonics $q = i = 1$ and $q = 1$, $i = -1$, i.e.,

$$\mathcal{P}_U^{\rm TM} = 4\pi\mathcal{P}_s\sum_{n=0}^{N-1}|{}_1^1I_n|^2 + 4\pi\mathcal{P}_s\sum_{n=0}^{N-1}\left|{}_{-1}^1I_n\right|^2. \tag{19}$$

Note from (11) that $|{}_1^1I_n| = \sqrt{2}k_p^2|P_1|^2$ and $|{}_{-1}^1I_n| = \sqrt{2}k_p^2|P_1||P_{-1}|$ with P_1 and P_{-1} being the positive and negative first-order Fourier coefficients of $p(t)$ (see (1)). Since $p(t)$ is real valued, its symmetric Fourier coefficients have the same modulus, which implies $|P_{-1}| = |P_1|$. Hence,

$$\mathcal{P}_U^{\rm TM} = 16\pi N\mathcal{P}_s k_p^4|P_1|^4 \tag{20}$$

and the time-modulation efficiency is

$$\eta_{\rm TM} = 4k_p^4|P_1|^4$$

[2]Recall that the array under study is composed of ideal isotropic elements, see paragraph below (6), and thus no conductive losses are included in the radiation efficiency computation.

Recalling that $k_p^2 = 1/5$ from the power normalization and that $|P_1| = \frac{2+2\sqrt{2}}{\pi}$, the final value of the time-modulation radiation efficiency is $\eta_{\rm TM} = 0.8928$, i.e., $\eta_{\rm TM}({\rm dB}) = -10\log_{10}(\eta_{\rm TM}) = 0.49$ dB.

The second parameter to be considered is the so-called hardware efficiency, $\eta_{\rm HW}$, which accounts for the insertion losses associated to the specific hardware elements selected for a TMA practical implementation. In our case, a hardware implementation of the SPDT module shown in Fig. 2 requires the following elements: a 3-way splitter, a 3-way combiner, three SPDT RF switches, and three time delay-lines for the π shifters. Determining $\eta_{\rm HW}$ is difficult due to the very different characteristics the hardware devices may have. To simplify, we will limit our study of $\eta_{\rm HW}$ to the representative frequencies $f_c = 2.5$ GHz (S band) and $f_c = 5.75$ GHz (C band) since virtually all TMA prototypes in the literature work in these bands (see [7, Table 1]).

On the other hand, the TMA fundamental frequency ($f_0 = 1/T_0$) must satisfy that $B_s < f_0 < f_{\rm SW}^{\rm speed}$ [6], with B_s the signal bandwidth and $f_{\rm SW}^{\rm speed}$ the maximum speed supported by the switches. Such a frequency restriction is necessary to achieve a twofold objective: a) to avoid spectral signal overlapping among the desired signal and the replicas generated by the TMA; and b) to ensure an appropriate time response of the switches. In this regard, $1/f_{\rm SW}^{\rm speed} = t_{\rm ON}+t_{\rm OFF}$ determines the switching speed, being $t_{\rm ON}$ ($t_{\rm OFF}$) the time period from 50% of the transition of the switch control signal to 90% (10%) of the detected RF output when the switch changes from an "off" ("on") state to an "on" ("off") state [3]–[5], [29]. Therefore, if we consider that $B_s = 5$ MHz, then, on the one hand, f_0 must be greater than 5 MHz (e.g., $f_0 = 5.5$ MHz) and, on the other, $f_{\rm SW}^{\rm speed}$ must exceed these 5.5 MHz. In other words, the selected switch must meet, in terms of speed, that $t_{\rm ON}+t_{\rm OFF} < 1/f_0 \approx 180$ ns.

After an exhaustive search among the most representative manufacturers of microwave devices, we selected the list of hardware elements shown in Table 2, which also provides their working frequencies and insertion losses. Such values will enable us to perform a realistic estimate of $\eta_{\rm HW}$ and make insightful comparisons with feeding networks constructed with conventional phased arrays (see Section V).

TABLE 2. Examples of devices working in the S and C frequency bands that can be used in a suitable implementation of the multibeam SSB TMA in Fig. 4.

Device	Frequency (GHz)	Insertion loss (dB)	Reference
2-way splitter/combiner	1.7-3 (S band)	$\eta_{\text{2-way}}$ =0.5	[28]
2-way splitter/combiner	5.5-6.5 (C band)	$\eta_{\text{2-way}}$ =0.5	[28]
3-way splitter/combiner	1.6-2.8 (S band)	$\eta_{\text{3-way}}$ =0.8	[28]
3-way splitter/combiner	4.4-5.9 (C band)	$\eta_{\text{3-way}}$ =1.2	[28]
SPDT RF switch	0.05-26.5	η_{SPDT} =0.4	[4]
SP3T RF switch	0.05-26.5	η_{SP3T} =0.5	[4]
time delay-line (PCB)	2.5±0.0025	$\eta_{\text{delay-line}}$ <0.06	[29]
time delay-line (PCB)	5.75±0.0025	$\eta_{\text{delay-line}}$ <0.08	[29]

The insertion losses of the time-delay lines correspond to their attenuation. Time-delay lines are typically constructed with printed circuit board (PCB) laminates, a technology that offers a good trade-off between cost and performance [28], [30]. Recall that when an electromagnetic wave is surrounded by insulating material other than the vacuum, its speed v_{PCB} is inversely proportional to the square root of the material's dielectric constant, D_k [31], i.e.,

$$v_{\text{PCB}} = \frac{c}{\sqrt{D_k}} \tag{21}$$

where c is the speed of light in vacuum. The inverse of the above expression is the propagation delay, t_{pd} [31],

$$t_{pd} = \frac{1}{v_{\text{PCB}}} = \frac{\sqrt{D_k}}{c}. \tag{22}$$

For a given carrier frequency f_c, the time delay t_π in seconds necessary to achieve a π-radian phase shift[3] should satisfy $2\pi f_c \cdot t_\pi = \pi$. Therefore, the ratio $L_{\text{delay}} = t_\pi / t_{pd}$ is the length in meters of the π-radian PCB delay line. Typically, PCB laminate manufacturers [28] provide attenuation charts per unit length for each frequency and, hence, the exact value for the attenuation –equivalently, for the delay line hardware efficiency, $\eta_{\text{delay-line}}$ (see Table 2)– can be finally obtained from L_{delay} and f_c. It is remarkable that, within the corresponding signal bandwidth, the variations of $\eta_{\text{delay-line}}$ are negligible.

Therefore, given the information in Table 2, the hardware efficiency (in dB) of the SPDT module in Fig. 2 is determined as follows

$$\eta^{\text{module}}_{\text{SPDT(dB)}} = 2\eta_{\text{3-way(dB)}} + \eta_{\text{SPDT(dB)}} + \eta_{\text{delay-line(dB)}}. \tag{23}$$

From this value we can obtain the hardware efficiency of the entire feeding network structure in Fig. 4 as

$$\eta_{\text{HW(dB)}} = 2\eta^{\text{module}}_{\text{SPDT(dB)}} + 2\eta_{\text{2-way(dB)}} + \eta_{\text{delay-line(dB)}}, \tag{24}$$

Finally, the overall SSB TMA efficiency (in dB) is

$$\eta_{\text{TMA(dB)}} = \eta_{\text{TM(dB)}} + \eta_{\text{HW(dB)}}. \tag{25}$$

where $\eta_{\text{TM(dB)}} = 0.49$ dB, as determined previously. Considering the insertion losses of the different devices shown in Table 2, we obtain the following values for the TMA efficiencies in the S and C bands

$$\begin{aligned} \eta_{\text{TMA(dB)}}|_{\text{S band}} &= 5.67\ \text{dB} \\ \eta_{\text{TMA(dB)}}|_{\text{C band}} &= 7.07\ \text{dB}. \end{aligned} \tag{26}$$

These are representative power efficiency values for the proposed SSB TMA in Fig. 4.

[3]Notice that the highest insertion losses for fixed phase shifters precisely correspond to π radians.

E. NUMERICAL SIMULATIONS

Let us consider a uniform linear SSB TMA with $N = 10$ elements spaced $\lambda_c/2$. We consider the two scenarios shown in Fig. 5 with different pointing directions, θ_a and θ_b, for the exploited harmonics. Pointing directions are $\theta_a = 80°$ and $\theta_b = 110°$ in the first scenario and $\theta_a = 75°$ and $\theta_b = 95°$ in the second one. Accordingly, the normalized time delays d_{1n} and d_{2n} are set in agreement with (17). On the one hand, we show that the proposed scheme is capable of concentrating the radiated power (recall that $\eta_{\text{TM}} = 89.3\%$) on the desired harmonic patterns, $|F^1_1(\theta)|^2$ and $|F^1_{-1}(\theta)|^2$, located at ω_c and $\omega_c + 2\omega_0$, respectively. The most meaningful

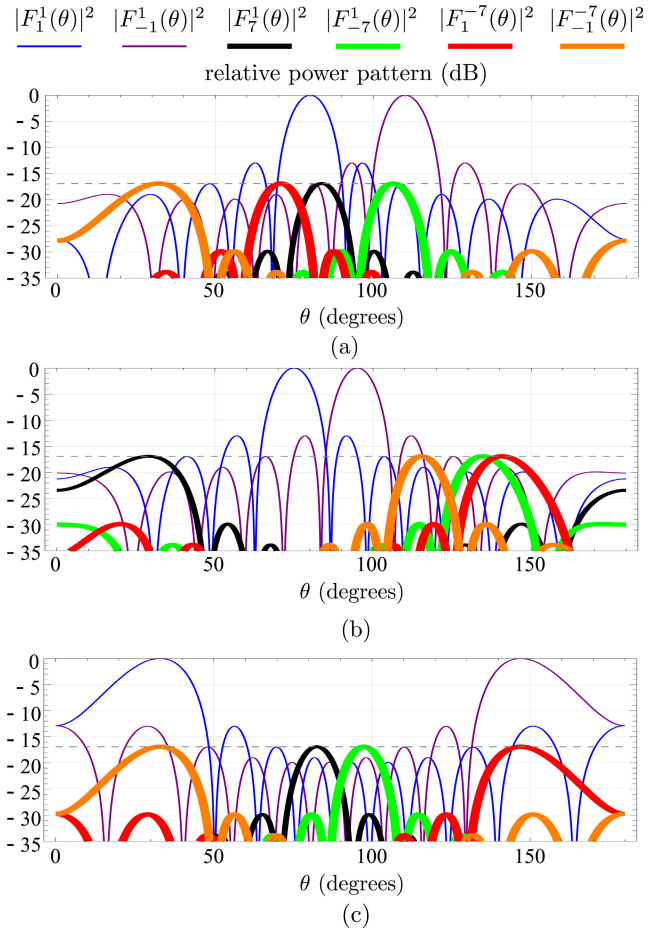

FIGURE 5. Beam patterns for the SSB TMA approach in Fig. 4. A uniform linear array with $N = 10$ elements is considered: (a) Scenario with the two useful beam patterns $F^1_1(\theta)$ and $F^1_{-1}(\theta)$ pointing to 80° and 110°, respectively. (b) Scenario with the two useful beam patterns pointing to 75° and 95°. (c) Simulations allowed us to verify that each useful harmonic beam pattern is able to support a scanning range of ±57° from the broad sight direction (i.e., [33°, 147°]). The figure shows a situation in which each beam is at one end of the scanning range. Unexploited harmonics always remain below −16.9 dB regardless of the selected pointing directions within such a range. Note that if instead of isotropic elements (or elements with an omnidirectional radiation pattern in the radiation plane under consideration), we had directional elements in that plane, it could not be guaranteed that the relative level of the undesired harmonics to that of the useful ones would remain constant over the entire scanning range.

unwanted harmonic patterns are the ones described in Table 1 and plotted with a thick line in Fig. 5.

It is remarkable that the highest (and common) peak level of the unwanted harmonics (−16.90 dB) is approximately 4 dB below the level of the main secondary lobes (−13 dB) of the desired patterns. Note that the values of d_{1n} and d_{2n} have no effect neither on the efficiency (see (21)) nor on the peak level of the unwanted harmonics. We have also found in the simulations that the scanning range of each beam is ±57° from broad sight direction and, whereas the threshold level of the unwanted harmonics is not being affected by the steering of the beams, the half power beam width of the corresponding exploited harmonic slightly widens as it moves away from the center. We have also verified that if N increases the scanning range is also increased (e.g., for $N = 30$, the scanning range is ±71°). On the other hand, as we are exclusively performing a phase weighting of the array excitations, the radiated power patterns shown in Fig. 5 are necessarily uniform.

Finally, we have analyzed the gain (in dBi) of each useful harmonic pattern given by:

$$G_{\text{eh}} = 10\log|\eta_{\text{TMA}}\frac{4\pi|F_{\text{eh}}(\theta_{\max})|^2}{\mathcal{P}^{\text{TM}}_{U_{\text{eh}}}}| \tag{27}$$

where F_{eh} is the spatial array factor at the exploited harmonic and $\mathcal{P}^{\text{TM}}_{U_{\text{eh}}}$ is the useful power radiated over such a harmonic. We represent in Fig. 6 the dependence of this gain with the number of elements of the array N (explicitly pointing out the case $N = 10$).

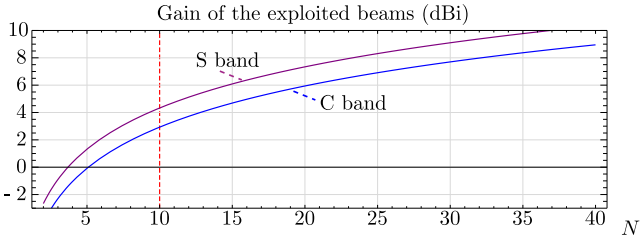

FIGURE 6. Gain of each exploited harmonic beam as a function of the number of array elements N (see (27)) in the frequency bands under study. We observe that for N=10 the gains are 4.3 dBi and 2.9 dBi in S and C bands, respectively.

III. ONE STATIC BEAM AND ONE STEERABLE BEAM

The second SSB TMA feeding network considered is constructed from two SP3T modules. In spite of its simplicity, it allows for handling one static beam pattern and one steerable beam pattern.

A. SP3T MODULE

Let us consider, again, a receive linear TMA with N ideal isotropic elements with unitary static excitations $I_n = 1, n \in \{0, 1, \ldots, N-1\}$. We will now consider that the array excitations are time modulated with the periodical (T_0) extension of the pulsed waveform $w(t)$ shown at the bottom of Fig. 7. Such a waveform is readily synthesized from the tri-state pulsed

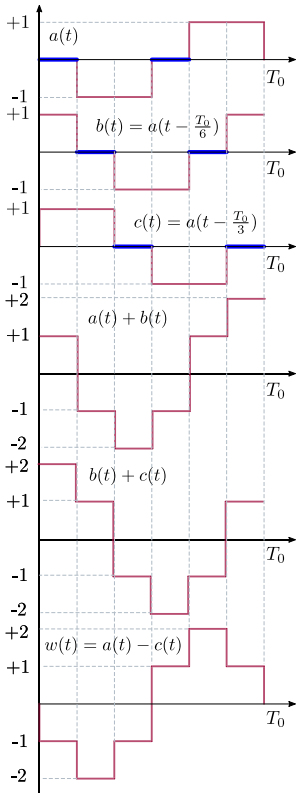

FIGURE 7. Single period (T_0) time-modulating tri-state pulsed waveforms $a(t)$, $b(t) = a(t - T_0/6)$, and $c(t) = a(t - 2T_0/6)$, and their linear combinations $w(t) = a(t) - c(t)$, $w(t - T_0/6) = b(t) + c(t)$, and $w(t - 2T_0/6) = a(t) + b(t)$.

waveform $a(t)$ and its time-shifted versions $b(t) = a(t - \frac{T_0}{6})$ and $c(t) = a(t - \frac{T_0}{3})$ (see Fig. 7). Time modulating with the tri-state signals $a(t)$, $b(t)$, and $c(t)$ is readily implementable with the SP3T switches shown in Fig. 8, which are controlled by the binary signals $g_1(t)$ and $g_2(t)$ as explained in Table 3. The working principle of the SP3T switches is the following: (1) if $g_1(t) = 0$ and $g_2(t) = 0$, the top output of the SP3T is selected and the $+1$ state of $a(t)$ is applied to the receive signal $s(t)$; (2) if $g_1(t) = 1$ and $g_2(t) = 0$, the middle output of the SP3T is selected and the -1 state of $a(t)$ is applied; and (3) if $g_1(t) = 0$ and $g_2(t) = 1$, the bottom output of the SP3T is selected and the 0 state of $a(t)$ is strategically utilized for directly receiving the signal $s(t)$. Time modulation with $b(t)$ and $c(t)$ is analogously implemented through the other two SP3T switches in Fig. 8, but governed by time-shifted versions of the same binary signals $g_1(t)$ and $g_2(t)$.

TABLE 3. Control inputs of the SP3T switch located on top of Fig. 8 and their effects on the received signal.

$g_1(t)$	$g_2(t)$	Throw	Effect on $s(t)$
0	0	top	$+1$ state
0	1	middle	-1 state
1	0	bottom	pass through

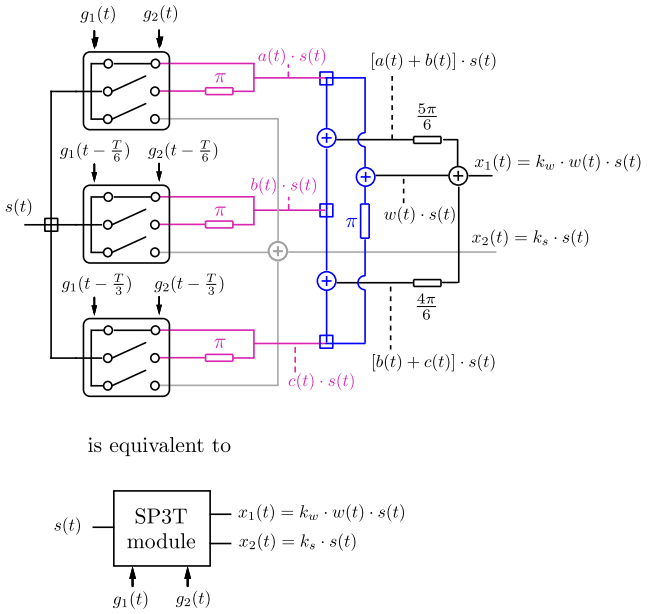

FIGURE 8. Feeding network with three SP3T switches (top) and its abstraction as a SP3T module (bottom).

The outputs of the three SP3T switches are combined as indicated in Fig. 8 to produce two outputs. One output is $x_1(t) = k_w w(t)s(t)$, the result of time modulating the input signal $s(t)$ by $w(t)$, being k_w a constant accounting for the possible attenuation values introduced by the feeding network. The second output results from the combination of the bottom outputs of the three SP3T switches (the gray lines in Fig. 8). Due to the particular time-multiplexed zero-states of $a(t)$, $b(t)$, and $c(t)$, which occupy the total period T_0 (see Fig. 7), we obtain a scaled version of the input signal, i.e., $x_2(t) = k_s s(t)$, being k_s the scaling constant, not affected by the time modulation and, hence, received over the fundamental mode.

The SP3T feeding network will be the building block of the SSB TMA approach considered in the ensuing subsection and, for this reason, it is abstracted in the block diagram named SP3T module shown in Fig. 8 (bottom).

The Fourier coefficients, W_q, of the periodical (T_0) extension of $w(t)$ are

$$W_q = \begin{cases} -\dfrac{3}{\mathrm{j}\pi q} & q \in \Upsilon \\ 0 & \text{otherwise,} \end{cases} \tag{28}$$

where $\Upsilon = \{\{6\Gamma - 1\} \cup \{6\Gamma - 5\}; \Gamma \in \mathbb{Z}\}$. The total time-averaged mean square value of $w(t)$ is

$$\mathcal{P}_w = \frac{1}{T_0}\int_0^{T_0} w^2(t)dt = \sum_{q\in\Upsilon} |W_q|^2 = 2 \tag{29}$$

Analogously to Section II, the SP3T module in Fig. 8 is able to deliver all the input power to the output when assuming that all the hardware elements in the module are ideal and have no insertion losses. Recalling $\mathcal{P}_s$ is the total time-averaged power of $s(t)$, the output power is distributed as $\frac{2}{3}\mathcal{P}_s$ and $\frac{1}{3}\mathcal{P}_s$ for the output signals $x_1(t)$ and $x_2(t)$, respectively. Hence, $k_w^2\mathcal{P}_w\mathcal{P}_s = \frac{2}{3}\mathcal{P}_s$ and $k_s^2\mathcal{P}_s = \frac{1}{3}\mathcal{P}_s$, which leads to $k_w = k_s = \frac{\sqrt{3}}{3}$.

B. SSB TMA FEEDING NETWORK

We now use the SP3T module introduced in the previous subsection as the building block of the SSB TMA feeding network shown in Fig. 9. Such a feeding network time modulates the signal received at the n-th antenna element by $h_n(t) = w(t-D_n)+\mathrm{j}w(t-D_n-\tau)$, where τ is chosen such that $\omega_0\tau = \pi/2$ and D_n is an adaptive time delay that will allow us to point the useful steerable harmonic beampattern towards a target direction. The time-variant array factor obtained with the feeding network in Fig. 9 (with $\mathrm{e}^{\mathrm{j}\omega_c t}$ explicitly included) is

$$F(\theta,t) = \frac{\sqrt{6}}{6}(1+\mathrm{j})\mathrm{e}^{\mathrm{j}\omega_c t}\sum_{n=0}^{N-1}\mathrm{e}^{\mathrm{j}\beta_c z_n\cos\theta} + \frac{\sqrt{6}}{6}\mathrm{e}^{\mathrm{j}\omega_c t}\sum_{n=0}^{N-1}h_n(t)\mathrm{e}^{\mathrm{j}\beta_c z_n\cos\theta}. \tag{30}$$

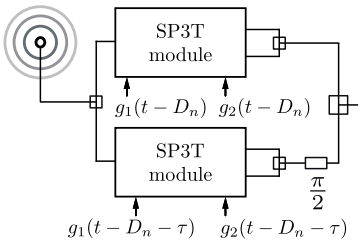

FIGURE 9. Block diagram of the n^{th} element feeding networks of the SSB TMA approach that allows to handle one static beam pattern and one steerable beam pattern.

Using the exponential Fourier series expansion of $w(t)$, the time-shifting property of the Fourier coefficients and $\mathrm{e}^{-\mathrm{j}q\omega_0\tau} = (-\mathrm{j})^q$, the time modulating signal $h_n(t)$ can be rewritten as

$$\begin{aligned} h_n(t) &= \sum_{q\in\Upsilon}\left[1-(-\mathrm{j})^{q+1}\right]W_q\mathrm{e}^{-\mathrm{j}q\omega_0 D_n}\mathrm{e}^{\mathrm{j}q\omega_0 t} \\ &= \sum_{q\in\Xi} 2W_q\mathrm{e}^{-\mathrm{j}q\omega_0 D_n}\mathrm{e}^{\mathrm{j}q\omega_0 t}, \end{aligned} \tag{31}$$

with $\Xi = \{\{12\Lambda - 7\} \cup \{12\Lambda - 11\}; \Lambda \in \mathbb{Z}\} = \{\cdots, -23, -19, -11, -7, 1, 5, 13, 17, \cdots\}$ being the indexes for which the Fourier coefficients of $h_n(t)$ are non-zero. Thus, the time-variant array factor (30) can be rewritten as

$$\begin{aligned} F(\theta,t) &= \frac{\sqrt{6}}{6}(1+\mathrm{j})\mathrm{e}^{\mathrm{j}\omega_c t}\sum_{n=0}^{N-1}\mathrm{e}^{\mathrm{j}\beta_c z_n\cos\theta} \\ &\quad + \frac{\sqrt{6}}{3}\sum_{q\in\Xi}\sum_{n=0}^{N-1}W_q\mathrm{e}^{-\mathrm{j}q\omega_0 D_n}\mathrm{e}^{\mathrm{j}\beta_c z_n\cos\theta}\mathrm{e}^{\mathrm{j}(\omega_c+q\omega_0)t} \\ &= F_0(\theta)\mathrm{e}^{\mathrm{j}\omega_c t} + \sum_{q\in\Xi}F_q(\theta)\mathrm{e}^{\mathrm{j}(\omega_c+q\omega_0)t} \end{aligned} \tag{32}$$

where $F_0(\theta) = \sum_{n=0}^{N-1} I_n^0 e^{j\beta_c z_n \cos\theta}$ and $F_q(\theta) = \sum_{n=0}^{N-1} I_n^q e^{j\beta_c z_n \cos\theta}$ are the spatial array factors at the frequencies ω_c and $\omega_c + q\omega_0$, respectively, with

$$I_n^0 = \frac{\sqrt{6}}{6}(1+j), \text{ and}$$
$$I_n^q = \frac{\sqrt{6}}{3} W_q e^{-jq\omega_0 D_n} \quad (33)$$

being the excitations associated to such patterns. Notice that the array excitations I_n^0 at the fundamental mode $q = 0$ are constant, and hence $F_0(\theta)$ has no steering ability. On the contrary, the excitations for $q \in \Xi$ are dynamic and, for a given q, the modulus $|I_n^q|$ is constant for all n, while the phases $\sphericalangle I_n^q$ depend linearly on D_n. Consequently, the array factors $F_q(\theta)$ have the same shape as a uniformly excited antenna array which is steerable towards a given direction determined by the delay parameter D_n.

Fig. 10 plots the amplitude of the normalized Fourier coefficients W_q where it can be observed that the most meaningful undesirable harmonics are those with order $|q| = 5$, which have a relative power level of -13.98 dB. Therefore, given the harmonics profile for $q \neq 0$ provided in Fig. 10, together with the fact that $10\log|I_n^0/I_n^1|^2 = 10\log\left(0.5/|W_1|^2\right) = -2.6$ dB,[4] we have that the most meaningful harmonic patterns in (32) are $F_0(\theta)$ (static) and $F_1(\theta)$ (steerable), at frequencies ω_c and $\omega_c + \omega_0$, respectively.

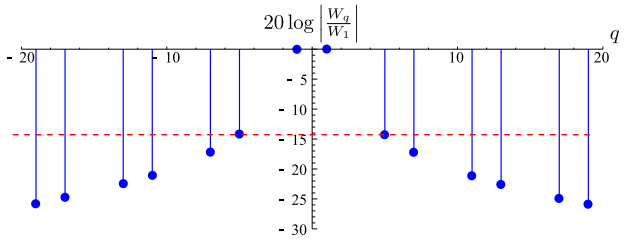

FIGURE 10. Normalized Fourier series mean square value spectrum in dB, $10\log_{10}\left|\frac{W_q}{W_1}\right|^2$, of the periodical extension of the stair-step pulse $w(t)$ in Fig. 7.

C. RADIATION AND HARDWARE EFFICIENCIES

We now determine the efficiency of the SP3T feeding network in Fig. 8. As in Section II, we will distinguish between the time-modulation radiation efficiency, η_{TM}, and the hardware efficiency, η_{HW}.

According to [9], the total power radiated by a SSB TMA is

$$\mathcal{P}_R^{\text{TM}} = 4\pi\mathcal{P}_s \sum_{n=0}^{N-1} |I_n^0|^2 + 4\pi\mathcal{P}_s \sum_{n=0}^{N-1} \sum_{q\in\Xi} |I_n^q|^2, \quad (34)$$

where $\mathcal{P}_s$ is the input power per antenna. Assuming unitary static excitations and ideal hardware elements without insertion losses (see Section III.A), the total power radiated simplifies to $\mathcal{P}_R^{\text{TM}} = 4\pi N\mathcal{P}_s$.

The useful power is the one radiated over the two harmonics $q = 0$ and $q = 1$, i.e.,

$$\mathcal{P}_U^{\text{TM}} = 4\pi\mathcal{P}_s \sum_{n=0}^{N-1} |I_n^0|^2 + 4\pi\mathcal{P}_s \sum_{n=0}^{N-1} |I_n^1|^2. \quad (35)$$

Bearing in mind (33) and (28), the useful power (35) is

$$\mathcal{P}_U^{\text{TM}} = 4\pi N\mathcal{P}_s \left(\frac{1}{3} + \frac{6}{\pi^2}\right) \quad (36)$$

and the time-modulation efficiency is

$$\eta_{\text{TM}} = \frac{\mathcal{P}_U^{\text{TM}}}{\mathcal{P}_R^{\text{TM}}} = \left(\frac{1}{3} + \frac{6}{\pi^2}\right) = 0.9413 \quad (37)$$

or $\eta_{\text{TM(dB)}} = -10\log_{10}(\eta_{\text{TM}}) = 0.26$ dB. It is interesting to note that this time-modulation radiation efficiency is higher than the one obtained for the SPDT TMA considered in Section II: 0.9413 versus 0.8928. This increase in the time-modulation efficiency is obtained at the expense of less steering flexibility since in the SP3T TMA only one beam is steerable.

Regarding the hardware efficiency of the SP3T module in Fig. 8, we have to distinguish between the hardware efficiency in the steerable beam output, $x_1(t)$, and in the static beam output, $x_2(t)$. Taking into account the hardware elements of a SP3T module and its corresponding insertion losses in Table 2, the steerable and static beam hardware efficiencies are, respectively,

$$\eta_{\text{SP3T(dB)}}^{\text{steerable}} = 2\eta_{\text{3-way(dB)}} + \eta_{\text{SP3T(dB)}} + 2\eta_{\text{2-way(dB)}} + 2\eta_{\text{delay-line(dB)}}$$
$$\eta_{\text{SP3T(dB)}}^{\text{static}} = 2\eta_{\text{3-way(dB)}} + \eta_{\text{SP3T(dB)}}, \quad (38)$$

and, hence, the overall hardware efficiency of the entire feeding network in Fig. 9 for each beam is

$$\eta_{\text{HW(dB)}}^{\text{steerable}} = \eta_{\text{SP3T(dB)}}^{\text{steerable}} + 3\eta_{\text{2-way(dB)}} + \eta_{\text{delay-line(dB)}}$$
$$\eta_{\text{HW(dB)}}^{\text{static}} = \eta_{\text{SP3T(dB)}}^{\text{static}} + 3\eta_{\text{2-way(dB)}} + \eta_{\text{delay-line(dB)}}, \quad (39)$$

leading to the following estimates for the overall TMA efficiencies (25) (see Table 2) for both beams and corresponding bands

$$\eta_{\text{TMA(dB)}}^{\text{steerable}}|_{\text{S band}} = \eta_{\text{TM(dB)}}^{\text{SP3T}} + \eta_{\text{HW(dB)}}^{\text{steerable}}|_{\text{S band}} = 5.04\,\text{dB},$$
$$\eta_{\text{TMA(dB)}}^{\text{static}}|_{\text{S band}} = \eta_{\text{TM(dB)}}^{\text{SP3T}} + \eta_{\text{HW(dB)}}^{\text{static}}|_{\text{S band}} = 2.61\,\text{dB},$$
$$\eta_{\text{TMA(dB)}}^{\text{steerable}}|_{\text{C band}} = \eta_{\text{TM(dB)}}^{\text{SP3T}} + \eta_{\text{HW(dB)}}^{\text{steerable}}|_{\text{C band}} = 5.90\,\text{dB}, \text{ and}$$
$$\eta_{\text{TMA(dB)}}^{\text{static}}|_{\text{C band}} = \eta_{\text{TM(dB)}}^{\text{SP3T}} + \eta_{\text{HW(dB)}}^{\text{static}}|_{\text{C band}} = 4.74\,\text{dB}. \quad (40)$$

D. NUMERICAL SIMULATIONS

Let us consider a uniform linear TMA with $N = 10$ elements spaced $\lambda_c/2$ with the SP3T SSB feeding network in Fig. 8. Fig. 11 shows the TMA array factors for the useful harmonics $F_0(\theta)$ (static) and $F_1(\theta)$ (steerable), and for the unwanted harmonics $F_q(\theta)$, $q = \{5, -7, -11\}$, normalized with respect to $F_1(\theta_{\max})$. It is apparent from this figure that the main lobes

[4] Notice that a better hardware efficiency of the static beam –not reflected in the radiation pattern in Fig. 11– compensates for the $10\log|I_n^0/I_n^1|^2 = -2.6$ dB, which improves to $-2.6 + (5.04 - 2.61) = -0.17$ dB for the S band, and $-2.6 + (5.90 - 4.74) = -1.44$ dB for the C band.

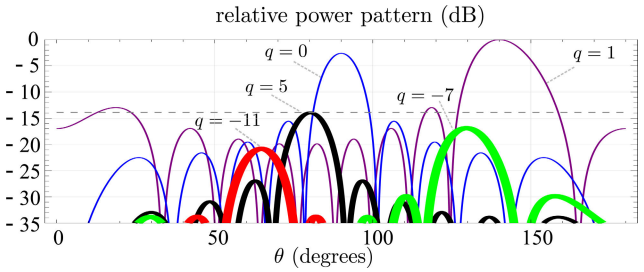

FIGURE 11. Beam patterns for the SSB TMA approach in Fig. 9. The useful beam patterns are at $q = 1$ (steerable by means of D_n and pointing to 140° in this figure), and at $q = 0$ (non-steerable). The most significant unwanted harmonics are at $q = \{5, -7, -11\}$ and they remain below −13.98 dB.

of the undesired harmonic patterns are kept below −13.98 dB, approximately 1 dB lower that the level of the main sidelobes (−13 dB) of the useful patterns. Fig. 11 also shows the 2.6 dB difference between the maximum of the useful radiation patterns $F_0(\theta_{\max})$ and $F_1(\theta_{\max})$.

We also found in the simulations (as in the SPDT SSB TMA of the previous section) that the scanning range of the steering beam is ±57° from broad sight direction. Finally, we represent in Fig. 12 the gain of each exploited harmonic beam as a function of the array elements N in the frequency bands under study.

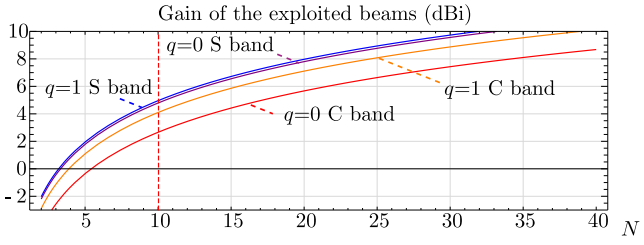

FIGURE 12. Gain of each exploited harmonic beam as a function of the number of array elements N (see (27)) in the frequency bands under study. We observe that for N=10 the gains are: in the S band: 4.7 dBi and 5.0 dBi for q=0 and $q = 1$, respectively, whereas in the C band: 2.6 dBi and 4.1 dBi for q=0 and $q = 1$, respectively.

IV. THREE INDEPENDENTLY-STEERABLE BEAMS

The third SSB TMA feeding network considered is the most complex one (see Fig. 13), involving three SPDT modules and two SP3T modules interconnected as in Fig. 13, but is capable of independently steering three array beam patterns. All switching modules use the same frequency ω_0, although three different delays (D_{1n}, D_{2n}, and D_{3n}).

Following a similar analysis as in Sections II and III, the time-varying array factor of the TMA being considered is

$$F(\theta,t) = \underbrace{\sum_{q\in\Xi}\sum_{i\ \text{odd}}\sum_{n=0}^{N-1} {}_i^qI_n \mathrm{e}^{\mathrm{j}\beta_c z_n\cos\theta}\mathrm{e}^{\mathrm{j}(\omega_c+(q+i)\omega_0)t}}_{\text{branch a}} + \underbrace{\sum_{m\in\Psi}\sum_{n=0}^{N-1} I_{mn}\mathrm{e}^{\mathrm{j}\beta_c z_n\cos\theta}\mathrm{e}^{\mathrm{j}(\omega_c+m\omega_0)t}}_{\text{branch b}}, \quad (41)$$

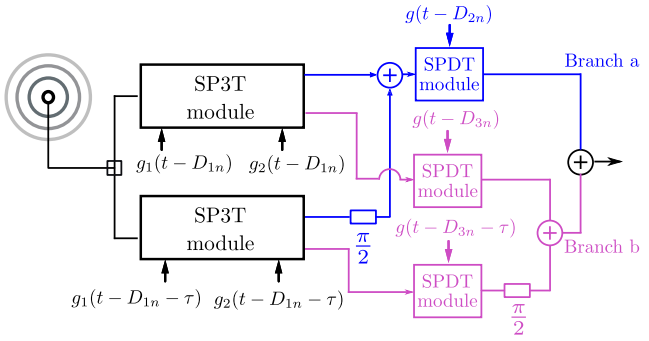

FIGURE 13. Block diagram of the n^{th} element feeding network of the SSB TMA approach that allows for steering independently three harmonic beam patterns.

where the dynamic excitations ${}_i^qI_n$ and I_{mn} are given by

$$ {}_i^qI_n = \sqrt{\frac{2}{15}}W_qP_i\cdot\mathrm{e}^{-\mathrm{j}\omega_0(qD_{1n}+iD_{2n})}$$
$$ I_{mn} = \sqrt{\frac{2}{15}}P_m\mathrm{e}^{-\mathrm{j}m\omega_0D_{3n}}. \quad (42)$$

These values of ${}_i^qI_n$ and I_{mn} are readily determined from the observation of the modules in branches a and b of the feeding network in Fig. 13.

Table 4 shows the most meaningful harmonic patterns in (41). The three harmonic beam patterns shaded in gray stand out from the others because of their significantly higher peak level. These are the harmonic beam patterns that will be considered useful for radiation while the rest will be treated as undesired. Note from Table 4 how the phases in the n-th antenna element of the three useful harmonics are determined by $D_{1n} + D_{2n}$, $D_{1n} - D_{2n}$, and D_{3n}, respectively. Note how this configuration has enough degrees of freedom to independently steer the direction of each useful beam pattern.

TABLE 4. Most meaningful harmonic beam patterns generated by the SSB TMA with the feeding network in Fig. 13. The useful harmonics are shaded in gray.

branch	q	i	frequency	dynamic excitations (${}_i^qI_n$)	${}_i^q\Delta_{\text{Peak}}$ (dB)
a	1	1	$\omega_c+2\omega_0$	$\sqrt{\frac{2}{15}}W_1P_1\cdot\mathrm{e}^{-\mathrm{j}\omega_0(D_{1n}+D_{2n})}$	−0.4
a	1	−1	ω_c	$\sqrt{\frac{2}{15}}W_1P_{-1}\cdot\mathrm{e}^{-\mathrm{j}\omega_0(D_{1n}-D_{2n})}$	−0.4
a	5	1	$\omega_c+6\omega_0$	$\sqrt{\frac{2}{15}}W_5P_1\cdot\mathrm{e}^{-\mathrm{j}\omega_0(5D_{1n}+D_{2n})}$	−14.4
a	5	−1	$\omega_c+4\omega_0$	$\sqrt{\frac{2}{15}}W_5P_{-1}\cdot\mathrm{e}^{-\mathrm{j}\omega_0(5D_{1n}-D_{2n})}$	−14.4
a	1	7	$\omega_c+8\omega_0$	$\sqrt{\frac{2}{15}}W_1P_7\cdot\mathrm{e}^{-\mathrm{j}\omega_0(D_{1n}+7D_{2n})}$	−17.3
a	1	−7	$\omega_c-6\omega_0$	$\sqrt{\frac{2}{15}}W_1P_{-7}\cdot\mathrm{e}^{-\mathrm{j}\omega_0(D_{1n}-7D_{2n})}$	−17.3

branch	m	–	frequency	dynamic excitations (I_{mn})	${}_i^q\Delta$Peak (dB)
b	1	–	$\omega_c+\omega_0$	$\sqrt{\frac{2}{15}}P_1\cdot\mathrm{e}^{-\mathrm{j}\omega_0D_{3n}}$	0
b	7	—	$\omega_c+7\omega_0$	$\sqrt{\frac{2}{15}}P_7\cdot\mathrm{e}^{-\mathrm{j}\omega_0 7D_{3n}}$	−16.9

Fig. 14 plots the radiation patterns of the most meaningful harmonics considered in Table 4 for a scenario in which the radiation pattern of the useful harmonics points towards the

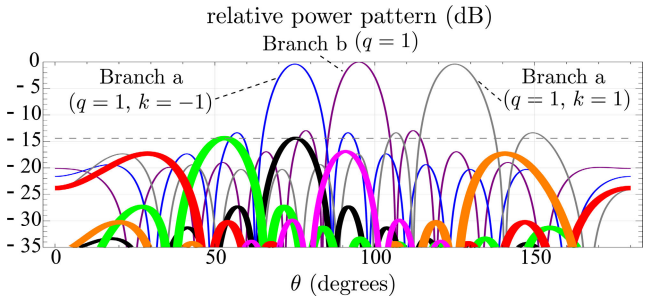

FIGURE 14. Beam patterns for the SSB TMA approach in Fig. 13. The useful patterns are the ones shaded in gray in Table 4 and point to 75°, 95°, and 125°, respectively. The most significant unwanted harmonics (see Table 4) are below −14.4 dB and the scanning range for each useful beam is [33°, 147°].

directions 75°, 95°, and 125°, respectively. Observe in Fig. 14 how the peak values of the radiation patterns of the unexploited harmonics are at least −14.4 dB below the peak values of the useful harmonics.

Regarding the efficiency, assuming unitary static excitations and ideal hardware elements without insertion losses (see Section III.A), the power radiated over the three useful harmonics is $\mathcal{P}_U^{\text{TM}} = 4\pi\mathcal{P}_s\left(\sum_{n=0}^{N-1}|{}_1^1I_n|^2 + |{}_{-1}^1I_n|^2 + |I_{1n}|^2\right)$, while the total power radiated is $\mathcal{P}_R^{\text{TM}} = 4\pi N\mathcal{P}_s$. Hence, from the dynamic excitations given by (42) and the Fourier coefficients given by (1) and (28), the time-modulation radiation efficiency $\eta_{\text{TM}} = \mathcal{P}_U^{\text{TM}}/\mathcal{P}_R^{\text{TM}}$ is

$$\begin{aligned}\eta_{\text{TM}} &= |{}_1^1I_n|^2 + |{}_{-1}^1I_n|^2 + |I_{1n}|^2 \\ &= \frac{2}{15}|P_1|^2(2|W_1|^2+1) \\ &= \frac{2}{15}\left(\frac{2+2\sqrt{2}}{\pi}\right)^2\left(2\left(\frac{3}{\pi}\right)^2+1\right) = 0.8894 \quad (43)\end{aligned}$$

or $\eta_{\text{TM}}(\text{dB}) = -10\log_{10}(\eta_{\text{TM}}) = 0.51$ dB.

In regard to the hardware efficiency, we will distinguish between the hardware efficiency in the branches a and b, namely

$$\begin{aligned}\eta_{\text{HW(dB)}}^{\text{branch a}} &= 3\eta_{\text{2-way(dB)}} + \eta_{\text{SP3T(dB)}}^{\text{steerable}} + \eta_{\text{SPDT(dB)}}^{\text{module}} \\ &\quad + \eta_{\text{delay-line(dB)}}, \\ \eta_{\text{HW(dB)}}^{\text{branch b}} &= 3\eta_{\text{2-way(dB)}} + \eta_{\text{SP3T(dB)}}^{\text{static}} + \eta_{\text{SPDT(dB)}}^{\text{module}} \\ &\quad + \eta_{\text{delay-line(dB)}}. \quad (44)\end{aligned}$$

Accordingly, an estimation of the overall TMA efficiency for each branch and frequency band is

$$\begin{aligned}\eta_{\text{TMA(dB)}}^{\text{branch a}}|_{\text{S band}} &= \eta_{\text{TM(dB)}} + \eta_{\text{HW(dB)}}^{\text{branch a}}|_{\text{S band}} = 7.35\,\text{dB}, \\ \eta_{\text{TMA(dB)}}^{\text{branch b}}|_{\text{S band}} &= \eta_{\text{TM(dB)}} + \eta_{\text{HW(dB)}}^{\text{branch b}}|_{\text{S band}} = 6.23\,\text{dB}, \\ \eta_{\text{TMA(dB)}}^{\text{branch a}}|_{\text{C band}} &= \eta_{\text{TM(dB)}} + \eta_{\text{HW(dB)}}^{\text{branch a}}|_{\text{C band}} = 9.05\,\text{dB}, \\ \eta_{\text{TMA(dB)}}^{\text{branch b}}|_{\text{C band}} &= \eta_{\text{TM(dB)}} + \eta_{\text{HW(dB)}}^{\text{branch b}}|_{\text{C band}} = 7.87\,\text{dB}. \quad (45)\end{aligned}$$

Finally, we represent in Fig. 15 the gain of each exploited harmonic beam as a function of the array elements N in the frequency bands under study.

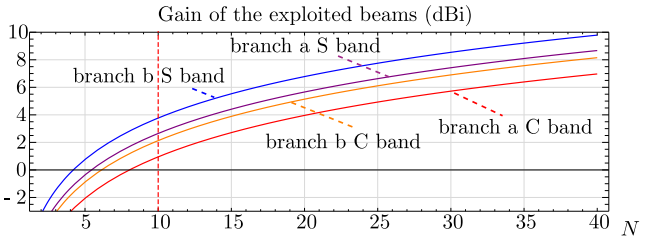

FIGURE 15. Gain of each exploited harmonic beam as a function of the number of array elements N (see (27)) in the frequency bands under study. We observe that for N=10 the gains are: in the S band: 2.6 dBi and 3.7 dBi for branch a and branch b useful harmonics, respectively, whereas in the C band: 0.9 dBi and 2.1 dBi for for branch a and branch b useful harmonics, respectively.

V. COMPARISON WITH STANDARD PHASED ARRAYS

In this section we compare the different multibeam SPMT TMA approaches considered in previous sections with standard multibeam phased arrays built with digital phase shifters. We focus on the approaches whose feeding networks are shown in Fig. 4 and 13, i.e., the ones which are able to provide two and three independently-steerable beams, respectively. Recall that TMA techniques provide almost continuous phase resolution based on controlling the switch-on instants (which determine the adaptive time delays D_{1n}, D_{2n}, and D_{3n}). Hence, in order to make a fair comparison with standard phased arrays, we consider high resolution (6 bits) digitally controlled phase shifters [3]–[5] (see Table 5) leading to phase steps of $\theta_{\text{step}} = 360°/2^6 = 5.6°$.

TABLE 5. Hardware devices used in standard multibeam phased arrays and their insertion losses for the S and C bands.

device	frequency (GHz)	insertion loss (dB)	reference
6-bit VPS	S band	$\eta_{\text{VPS}} = 4.64$	[3]–[5]
6-bit VPS	C band	$\eta_{\text{VPS}} = 5.83$	[4], [5]
2-way split./combiner	1.7 − 3 (S band)	$\eta_{\text{2-way}} = 0.5$	[28]
2-way split./combiner	5.5 − 6.5 (C band)	$\eta_{\text{2-way}} = 0.5$	[28]
3-way split./combiner	1.6 − 2.8 (S band)	$\eta_{\text{3-way}} = 0.8$	[28]
3-way split./combiner	4.4 − 5.9 (C band)	$\eta_{\text{3-way}} = 1.2$	[28]

The comparison focuses on four aspects: power efficiency, phase sensitivity, complexity, and cost effectiveness:

- **Power efficiency**: In order to determine the power efficiency of a phased array feeding network, we have considered the average insertion losses (η_{VPS}) of 6-bit monolithic microwave integrated circuit (MMIC) commercial VPS [3]–[5] shown in Table 5 for the bands S and C, respectively. Accordingly, we have the following phased array (PA) power efficiencies in the S band (see Table 5)

$$\begin{aligned}\eta_{\text{PA(dB)}}^{\text{2 beams}}|_{\text{S band}} &= 2\eta_{\text{2-way(dB)}}|_{\text{S band}} + \eta_{\text{VPS(dB)}}|_{\text{S band}} \\ &= 5.64\,\text{dB} \\ \eta_{\text{PA(dB)}}^{\text{3 beams(dB)}}|_{\text{S band}} &= 2\eta_{\text{3-way(dB)}}|_{\text{S band}} + \eta_{\text{VPS(dB)}}|_{\text{S band}} \\ &= 6.24\,\text{dB} \quad (46)\end{aligned}$$

TABLE 6. Performance comparison in terms of efficiency, phase sensitivity, complexity, and cost-effectiveness between the proposed two and three independently-steerable beams SSB TMA approaches (in boldface) and standard phased arrays with 6-bit digital VPS for the S and C bands [3]–[5].

		proposed TMAs vs. standard phased arrays with 6-bit VPSs					
	frequency band	η(dB)	$\theta_{\text{step}}(^\circ)$	$\theta_{\text{error}}^{\text{RMS}}(^\circ)$	**switches/beam**	**splitters/beam**	**TMA cost savings (%)**
2 beams	S	**5.7** vs. 5.6	**1.7** vs. 5.6	**0.3** vs. 2.2	**4.5** vs. 12	**4** vs. 1	**114.2**
2 beams	C	**7.3** vs. 6.8	**1.7** vs. 5.6	**0.3** vs. 3.3	**4.5** vs. 12	**4** vs. 1	**130.4**
3 beams	S	**7.6** vs. 6.2	**1.7** vs. 5.6	**0.3** vs. 2.2	**5** vs. 12	**9.3** vs. 0.7	**42.4**
3 beams	C	**9.3** vs. 8.2	**1.7** vs. 5.6	**0.3** vs. 3.3	**5** vs. 12	**9.3** vs. 0.7	**49.5**

whereas in the C band, we have

$$\begin{aligned}\eta_{\text{PA(dB)}}^{\text{2 beams(dB)}}|_{\text{C band}} &= 2\eta_{\text{2-way(dB)}}|_{\text{C band}}+\eta_{\text{VPS(dB)}}|_{\text{C band}}\\ &= 6.83\,\text{dB}\\ \eta_{\text{PA(dB)}}^{\text{3 beams(dB)}}|_{\text{C band}} &= 2\eta_{\text{3-way(dB)}}|_{\text{C band}}+\eta_{\text{VPS(dB)}}|_{\text{C band}}\\ &= 8.23\,\text{dB}\end{aligned} \tag{47}$$

From Table 6 we observe that TMAs and phased arrays have similar power efficiencies with differences always below 0.6 dB (or 8.6%) for the two-beams feeding network. For the case of three beams, the difference is slightly larger (below 1.4 dB (or 18.0%) in any case) due to the presence of a greater number of power splitters/combiners.

- **Phase sensitivity**: the phase step, θ_{step}, and the root mean square (RMS) phase error, $\theta_{\text{error}}^{\text{RMS}}$, determine the phase sensitivity of an steering array. Notice that, by using progressive phases in the TMA excitations (assuming N elements spaced $\lambda_c/2$ apart), if we want to steer a certain useful harmonic beampattern towards the direction θ_p, the time delays in the n-th array element modulating signal, τ_n, must satisfy [20]

$$\tau_n = \pi n\cos(\theta_p)/\omega_0;\ n\in\Psi=\{0,\cdots,N-1\}, \tag{48}$$

and hence the θ_p derivative with respect to t in absolute value is given by

$$\frac{\partial\theta_p}{\partial t} = \frac{2}{nT_0\sin\theta_p}\frac{\partial\tau_n}{\partial t}, \tag{49}$$

and we realize that the most restrictive conditions to determine θ_{step} from $\partial\theta_p/\partial t$ are: $n=1$, $\sin\theta_p$ reaching its minimum in the scanning range (i.e., for $\theta_p = 33^\circ$ in all TMA approaches), and $\partial\tau_n/\partial t = t_{\text{RF}}^{\text{sw}}$ (which determines the switching speed since it is the time from 10% to 90% of detected RF voltage, which in our case is 50 ns [4]), yielding $\theta_{\text{step}} = 1.7^\circ$ versus 5.6° in 6-bit VPSs (see Table 6). Notice that $\theta_{\text{step}} = 1.7^\circ$ is approximately that of an 8-bit VPS. Additionally, we determine the RMS phase error within the scanning range $(\theta_{\min}^s, \theta_{\max}^s)$ by means of

$$\theta_{\text{error}}^{\text{RMS}} = \sqrt{\frac{1}{\theta_{\max}^s-\theta_{\min}^s}\int_{\theta_{\min}^s}^{\theta_{\max}^s}\left|\frac{\partial\theta_p}{\partial t}\right|_{n=1}^2 d\theta_p}, \tag{50}$$

obtaining $\theta_{\text{error}}^{\text{RMS}} = 0.3^\circ$ for both frequency bands S and C, while $\theta_{\text{error}}^{\text{RMS}} = 2.2^\circ$ (band S) and $\theta_{\text{error}}^{\text{RMS}} = 3.3^\circ$ (band C) for 6-bit VPSs. Table 6 reflects the average values of θ_{step} and $\theta_{\text{error}}^{\text{RMS}}$ for 6-bit commercial VPSs. We must clarify that, for higher TMA f_0 values, lower $t_{\text{RF}}^{\text{sw}}$ values are required, hence θ_{step} (and $\theta_{\text{error}}^{\text{RMS}}$) improves at the expense of both a worse η_{TMA} and cost-effectiveness. In any case, ultra-fast switch prototypes ($t_{\text{RF}}^{\text{sw}} < 0.1$ ns) at very high frequencies (up to 70 GHz) are already available [32], and it remains to see how high the costs of an off-the-shelf integrated circuit implementation are.

- **Complexity**: we analyzed complexity in terms of the two most abundant elements in a multibeam feeding network: switches and power splitter/combiners. Notice that a b-bit digital phase shifter usually employs $2b$ SPDT switches [3]–[5]. Particularly, we considered the number of switches and power splitter/combiners employed per beam in the proposed TMAs and phased arrays. We found (see Table 6) that the proposed TMAs are advantageous in terms of the number of switches, but they require more power splitter/combiners (especially for the three beams case). This fact could be a disadvantage for increasing frequencies since the cost of such devices also increases.
- **Cost-effectiveness**: for the analyzed frequency bands (2 − 8 GHz), and for the considered signal bandwidth (5 MHz), the miniaturization of integrated circuits allows the proposed TMAs to be a competitive alternative to phased arrays in terms of cost. The margin gets wider as the frequency increases in all cases, although differences are smaller for the case of three beams due to the higher number of power splitters/combiners. More specifically, technologies such as heterolithic microwave integrated circuit (HMIC) applied to RF switches [4], MMICb and low temperature co-fired ceramic (LTCC) to power splitter/combiners [27], or PCB laminates [28] to fixed delay lines are crucial to this comparative advantage of multibeam TMAs at these frequency bands. For higher frequencies, although the insertion losses of Wilkinson power splitters/combiners remain low, the prices are high [33].

VI. CONCLUSION AND FURTHER INVESTIGATIONS

In this paper we have proposed and analyzed three different multibeam SSB TMA feeding networks with adaptive steerable capabilities. The feeding networks result from different combinations of several modules constructed with SPDT and

SP3T switches, which are significantly more versatile and power efficient than the SPST switches employed in conventional TMAs. The proposed multibeam SSB TMA feeding networks are compared with those of standard phased arrays implemented with digitally controlled VPSs and shown to exhibit a similar overall power efficiency, a better phase resolution response, and an excellent competitive advantage in terms of cost.

In any case, we are aware that, after this analysis, a series of natural research lines remain open such as full-wave simulations with nonideal antenna elements as well as the subsequent implementation and testing of the corresponding prototypes.

REFERENCES

[1] P. Rocca, G. Oliveri, R. J. Mailloux, and A. Massa, "Unconventional phased array architectures and design Methodologies—A review," *Proc. IEEE*, vol. 104, no. 3, pp. 544–560, Mar. 2016.
[2] R. Maneiro-Catoira, J. Brégains, J. A. García-Naya, and L. Castedo, "Time modulated arrays: From their origin to their utilization in wireless communication systems," *Sensors*, vol. 17, no. 3, pp. 1–14, Mar. 2017.
[3] *Qorvo*. Accessed: Mar. 1, 2020. [Online]. Available: http://www.qorvo.com,SP3Tswitches.RF1628
[4] *Macom*. MMICdigital phase shifters and SPMT Switches: MASW-00x100 Series. Accessed: Mar. 1, 2020. [Online]. Available: https://www.macom.com
[5] *Analog Devices*. SPDT Switches, DVariable Phase Shifters. HMC545A. HMC649A, HMC642A. Accessed: Mar. 1, 2020. [Online]. Available: https://www.analog.com
[6] R. Maneiro-Catoira, J. C. Bregains, J. A. Garcia-Naya, and L. Castedo, "On the feasibility of time-modulated arrays for digital linear modulations: A theoretical analysis," *IEEE Trans. Antennas Propag.*, vol. 62, no. 12, pp. 6114–6122, Dec. 2014.
[7] G. Bogdan, K. Godziszewski, Y. Yashchyshyn, C. H. Kim, and S. Hyun, "Time modulated antenna array for real-time adaptation in wideband wireless systems—Part I: Design and characterization," *IEEE Trans. Antennas Propag.*, early access, Mar. 4, 2019, doi: 10.1109/TAP.2019.2902755.
[8] Q. Chen, J.-D. Zhang, W. Wu, and D.-G. Fang, "Enhanced single-sideband time-modulated phased array with lower sideband level and loss," *IEEE Trans. Antennas Propag.*, vol. 68, no. 1, pp. 275–286, Jan. 2020.
[9] R. Maneiro-Catoira, J. C. Bregains, J. A. Garcia-Naya, L. Castedo, P. Rocca, and L. Poli, "Performance analysis of time-modulated arrays for the angle diversity reception of digital linear modulated signals," *IEEE J. Sel. Topics Signal Process.*, vol. 11, no. 2, pp. 247–258, Mar. 2017.
[10] C. He, X. Liang, B. Zhou, J. Geng, and R. Jin, "Space-division multiple access based on time-modulated array," *IEEE Antennas Wireless Propag. Lett.*, vol. 14, pp. 610–613, 2015.
[11] R. Maneiro-Catoira, M. B. Angoue Avele, J. Bregains, J. A. Garcia-Naya, and L. Castedo, "Multibeam transceiver with 4d arrays based on single-pole multiple-throw switches," in *Proc. WSA 23rd Int. ITG Workshop Smart Antennas*, Apr. 2019, pp. 1–5.
[12] C. He, X. Liang, Z. Li, J. Geng, and R. Jin, "Direction finding by time-modulated array with harmonic characteristic analysis," *IEEE Antennas Wireless Propag. Lett.*, vol. 14, pp. 642–645, 2015.
[13] C. He, A. Cao, J. Chen, X. Liang, W. Zhu, J. Geng, and R. Jin, "Direction finding by time-modulated linear array," *IEEE Trans. Antennas Propag.*, vol. 66, no. 7, pp. 3642–3652, Jul. 2018.
[14] Q. Zhu, S. Yang, R. Yao, and Z. Nie, "Directional modulation based on 4-D antenna arrays," *IEEE Trans. Antennas Propag.*, vol. 62, no. 2, pp. 621–628, Feb. 2014.
[15] P. Rocca, Q. Zhu, E. T. Bekele, S. Yang, and A. Massa, "4-D arrays as enabling technology for cognitive radio systems," *IEEE Trans. Antennas Propag.*, vol. 62, no. 3, pp. 1102–1116, Mar. 2014.
[16] G. Li, S. Yang, Y. Chen, and Z.-P. Nie, "A novel electronic beam steering technique in time modulated antenna array," *Prog. Electromagn. Res.*, vol. 97, pp. 391–405, 2009.
[17] S. Yang, Y. B. Gan, and P. K. Tan, "Evaluation of directivity and gain for time-modulated linear antenna arrays," *Microw. Opt. Technol. Lett.*, vol. 42, no. 2, pp. 167–171, 2004.
[18] L. Poli, P. Rocca, G. Oliveri, and A. Massa, "Harmonic beamforming in time-modulated linear arrays," *IEEE Trans. Antennas Propag.*, vol. 59, no. 7, pp. 2538–2545, Jul. 2011.
[19] G. Bogdan, Y. Yashchyshyn, and M. Jarzynka, "Time-modulated antenna array with lossless switching network," *IEEE Antennas Wireless Propag. Lett.*, vol. 15, pp. 1827–1830, 2016.
[20] R. Maneiro-Catoira, J. Brégains, J. A. García-Naya, and L. Castedo, "Time-modulated array beamforming with periodic stair-step pulses," *Signal Process.*, vol. 166, Jan. 2020, Art. no. 107247.
[21] A.-M. Yao, W. Wu, and D.-G. Fang, "Single-sideband time-modulated phased array," *IEEE Trans. Antennas Propag.*, vol. 63, no. 5, pp. 1957–1968, May 2015.
[22] Y. Tong and A. Tennant, "A two-channel time modulated linear array with adaptive beamforming," *IEEE Trans. Antennas Propag.*, vol. 60, no. 1, pp. 141–147, Jan. 2012.
[23] G. Li, S. Yang, and Z. Nie, "Direction of arrival estimation in time modulated linear arrays with unidirectional phase center motion," *IEEE Trans. Antennas Propag.*, vol. 58, no. 4, pp. 1105–1111, Apr. 2010.
[24] J. C. Bregains, J. Fondevila-Gomez, G. Franceschetti, and F. Ares, "Signal radiation and power losses of time-modulated arrays," *IEEE Trans. Antennas Propag.*, vol. 56, no. 6, pp. 1799–1804, Jun. 2008.
[25] S. Yang, Y. Beng Gan, and A. Qing, "Sideband suppression in time-modulated linear arrays by the differential evolution algorithm," *IEEE Antennas Wireless Propag. Lett.*, vol. 1, pp. 173–175, 2002.
[26] J. P. Gonzalez-Coma, R. Maneiro-Catoira, and L. Castedo, "Hybrid precoding with time-modulated arrays for mmwave MIMO systems," *IEEE Access*, vol. 6, pp. 59422–59437, 2018.
[27] *Minicircuits*. Accessed: Mar. 1, 2020. [Online]. Available: http://www.minicircuits.com,powersplitters/dividers:SCG-3-592+,WP4F1+
[28] *Rogers*. Accessed: Mar. 1, 2020. [Online]. Available: https://www.rogerscorp.com,rO4000 hydrocarbonceramiclaminates
[29] *Understanding Rf/Microwave Solid State Switches and Their Applications*. keysight Application Note. Accessed: Apr. 4, 2020. [Online]. Available: http://www.keysight.com/us/en/assets/7018-01705/application-notes/5989-7618.pdf
[30] A. M. Abbosh, "Broadband fixed phase shifters," *IEEE Microw. Wireless Compon. Lett.*, vol. 21, no. 1, pp. 22–24, Jan. 2011.
[31] *What is a PCB Transmission Line*. Sierra Circuits. Accessed: Apr. 4, 2020. [Online]. Available: https://www.protoexpress.com/blog/pcb-transmission-line/
[32] M. Thian and V. F. Fusco, "Ultrafast low-loss 42–70 GHz differential SPDT switch in 0.35 μm SiGe technology," *IEEE Trans. Microw. Theory Techn.*, vol. 60, no. 3, pp. 655–659, Mar. 2012.
[33] *Knowles*. Accessed: Apr. 4, 2020. Wilkinson Power Dividers: PDW06398, PDW06399, PDW08605. [Online]. Available: https://www.knowlescapacitors.com

ROBERTO MANEIRO-CATOIRA (Member, IEEE) received the degree in telecommunications engineering from the University of Vigo, Spain, in 1995, and the master's degree in information and telecommunications technologies for mobile networks and the Ph.D. degree from the University of A Coruña, Spain, in 2012 and 2017, respectively. From 1996 to 1997, he was with Egatel Company focused on the research and development in TV and radio digital communications. From 1997 to 2000, he was with Siemens Mobile Networks as a GSM Access Network Deployment Manager. From 2000 to 2003, he was with Nortel Networks as an UMTS Network Integration Manager. Since 2003, he has been teaching siemens simatic programmable logic devices and mathematics for different levels of private and public organizations. Since 2017, he has been a Researcher with the Electronic Technology and Communications Group, University of A Coruña. His research interest includes smart antenna technologies.

JOSÉ A. GARCÍA-NAYA (Senior Member, IEEE) received the degree in computer engineering and the M.Sc. and Ph.D. degrees from the University of A Coruña (UDC), A Coruña, Spain, in 2005 and 2010, respectively. Since 2005, he has been with the Group of Electronics Technology and Communications, UDC, where he is currently an Associate Professor. He is also a member of the research team in more than 40 research projects funded by the public organizations and private companies. He is the coauthor of more than 90 peer-reviewed papers in journals and conferences. His research interests include signal processing for wireless communications, wireless sensor networks, specially devoted to indoor positioning systems, time-modulated antenna arrays applied to wireless communication systems, and experimental evaluation of wireless systems in realistic scenarios, such as indoors, outdoors, high-mobility, railway transportation, and so on.

JULIO C. BRÉGAINS (Senior Member, IEEE) received the B.S. degree in electrical engineering from the National University of the Northeast, Argentina, in 2000, the degree in industrial engineering from the University of León, Spain, in 2006, and the Ph.D. degree (Hons.) in applied physics from the University of Santiago de Compostela (USC), Spain, in 2007. He is currently an Assistant Professor of electronics with the Department of Electronics and Systems, School of Informatics, University of A Coruña, Spain. He is also a member of the Electronic Technology and Communications Group (GTEC), Department of Electronics and Systems. He has coauthored over 80 international journal and conference papers and received awards for three of them. His research interests include high-frequency electronics, software development for solving electromagnetic problems, antenna array pattern synthesis and design, and variation problems applied to field theory.

LUIS CASTEDO (Senior Member, IEEE) received the Ph.D. degree in telecommunications engineering from the Technical University of Madrid, Spain, in 1993. Since 1994, he has been a Faculty Member with the Department of Computer Engineering, University of A Coruña (UDC), Spain, where he was a Professor, in 2001, and the Chairman, from 2003 to 2009. He held several research appointments with the École supérieure d'électricité (SUPELEC) and the University of Southern California (USC). From 2014 to 2018, he was a Manager with the Communications and Electronic Technologies (TEC) Program, State Research Agency, Spain. He was also a Principal Researcher of more than 50 research projects funded by the public organisms and private companies. He has coauthored more than 300 papers in peer-reviewed international journals and conferences. His research interests include signal processing for wireless communications and prototyping of digital communication equipment. His articles received three Best Student Paper Awards from the IEEE/ITG Workshop on Smart Antennas in 2007, the IEEE International Workshop on Signal Processing Advances in Wireless Communications in 2013, and the IEEE International Conference on Internet of Things (iThings) in 2017. He served as the General Co-Chair for the 8th IEEE Sensor Array and Multichannel Signal Processing Workshop in 2014 and the 27th European Signal Processing Conference in 2019.